

THE MILKY WAY'S KILOPARSEC SCALE WIND: A HYBRID COSMIC-RAY AND THERMALLY DRIVEN OUTFLOW

BY JOHN E. EVERETT^{1,2,3}, ELLEN G. ZWEIBEL^{1,2,3}, ROBERT A. BENJAMIN⁴,
DAN MCCAMMON², LINDSAY ROCKS²,
JOHN S. GALLAGHER, III¹

Accepted for publication to ApJ

ABSTRACT

We apply a wind model, driven by combined cosmic-ray and thermal-gas pressure, to the Milky Way, and show that the observed Galactic diffuse soft X-ray emission can be better explained by a wind than by previous static gas models. We find that cosmic-ray pressure is essential to driving the observed wind. Having thus defined a “best-fit” model for a Galactic wind, we explore variations in the base parameters and show how the wind’s properties vary with changes in gas pressure, cosmic-ray pressure and density. We demonstrate the importance of cosmic rays in launching winds, and the effect cosmic rays have on wind dynamics. In addition, this model adds support to the hypothesis of Breitschwerdt and collaborators that such a wind may help explain the relatively small gradient observed in γ -ray emission as a function of galactocentric radius.

Subject headings: ISM:outflows – ISM:cosmic rays – ISM:magnetic fields – Galaxy:evolution – X-rays:diffuse background

1. INTRODUCTION

Large-scale galactic outflows are usually considered in the context of starburst galaxies or Active Galactic Nuclei (Veilleux et al. 2005). These outflows are interesting not only intrinsically (what drives the outflow?) but for the interstellar and intergalactic media (how is the host galaxy affected, and what metals are ejected from the galaxy?).

To examine these questions, we have built a thermal and cosmic-ray driven wind model. Our investigation into such models was first inspired by observational hints that the Milky Way may possess a kiloparsec-scale wind; this paper further explores that possibility. To motivate this study, we first introduce the observational evidence for a Galactic wind (§§1.1 and 1.2) and then introduce the cosmic-ray and thermally driven wind model (§2). In §3, we calculate the X-ray emission from this wind, and then compare it to the observations. After finding the best-fit wind model, we then explore the parameter space around that model (§4) to understand more about how the wind is modified by varying the input and fit parameters. Our conclusions are given in §5.

But first, observational hints for an outflow from our own Galaxy.

1.1. X-ray Observations

The Milky Way does exhibit clues that it might drive a large-scale wind. The first of these is an enhancement in the diffuse soft X-ray emission, stretching over the longitude range $-20^\circ \lesssim l \lesssim 35^\circ$ with an emission scale height in the southern Galactic hemisphere of $b \sim -17^\circ$ (see Fig. 1). This emission was first noted by Snowden et al. (1995), who modeled it with an isothermal plasma with a temperature $T =$

4×10^6 K, a midplane electron density of $n_{e,\text{midplane}} \sim 3.5 \times 10^{-3} \text{ cm}^{-3}$, and a midplane thermal pressure of $P_{g,\text{midplane}}/k \sim 2.8 \times 10^4 \text{ cm}^{-3} \text{ K}$. At approximately the same time, Breitschwerdt & Schmutzler (1994) suggested that the average *all-sky* X-ray emission (not only that emission in the region defined above) in all *ROSAT* bands might be explained by delayed-recombination in a large-scale cosmic-ray and thermally driven wind (see also Breitschwerdt & Schmutzler 1999).

Later, Almy et al. (2000) used intervening absorption to show that at least half of the central, enhanced X-ray emission lies more than 2 kpc from the sun (see also Park et al. 1997, 1998). Since that measurement was made in the Galactic plane, where the absorption is strongest, it was inferred that most of the emission observed at higher latitudes lies beyond that 2 kpc distance. Almy et al. (2000) also improved on previous modeling efforts: that work presents a model of the emission due to a static polytropic gas (with $\gamma = 5/3$), and very importantly, includes the effects of known background components, such as the stellar background, extragalactic background, and an additional isotropic background (to fit high-latitude emission). For comparison, their model had a central temperature of $T_0 = 8.2 \times 10^6$ K, a central electron density of $n_e = 1.1 \times 10^{-2} \text{ cm}^{-3}$, and a central pressure of $P_{g,0} = 1.8 \times 10^5 \text{ cm}^{-3} \text{ K}$.

We will compare our results with this static polytrope model to investigate whether a wind model for this emission is feasible.

1.2. Cosmic Ray Source Density

Another indicator of a Galactic wind comes from measurements of the density of cosmic rays as a function of Galactocentric radius, R . The source density of cosmic rays can be determined via γ -ray emission: the production of γ -ray photons with energies exceeding about 50 MeV is dominated by collisions of cosmic rays with gas in the interstellar medium (Bloemen et al. 1984). Since the galaxy is largely transparent to such high-energy photons, the γ -ray emissivity at those energies yields the cosmic ray source density.

If cosmic rays are produced in supernovae remnants, then

Electronic address: everett@physics.wisc.edu

¹ University of Wisconsin–Madison, Department of Astronomy, 475 N. Charter, Madison, WI 53706

² University of Wisconsin–Madison, Department of Physics, 425 N. Charter, Madison, WI 53706

³ Center for Magnetic Self-Organization in Laboratory and Astrophysical Plasmas

⁴ University of Wisconsin–Whitewater, Department of Physics, 800 West Main Street, Whitewater, WI 53190

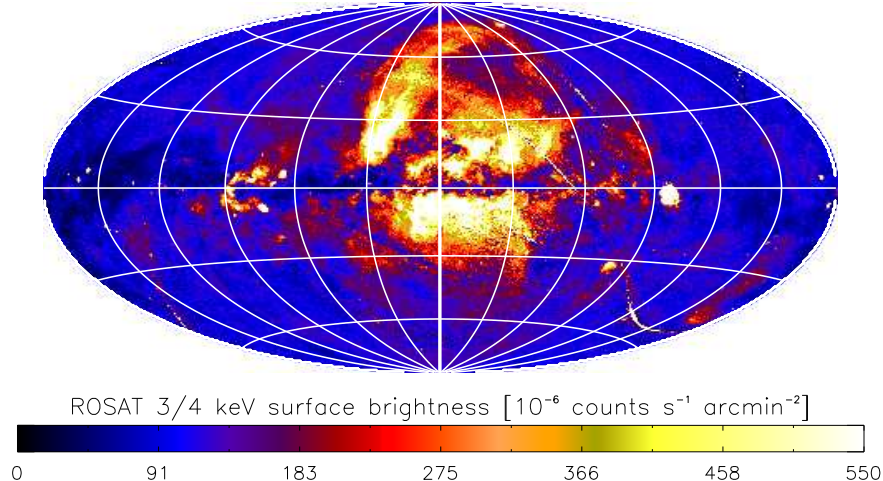


FIG. 1.— X-ray emission at 3/4 keV (the “R45 band”) as seen by *ROSAT* (Snowden et al. 1997). These observations suggest a “Galactic X-ray Bulge”, seen most clearly in the southern Galactic Hemisphere, and stretching over the Galactic longitude range, l , from $|l| \lesssim 30^\circ$ and down to approximately -15° in Galactic latitude. This paper asks whether the X-ray bulge in the southern Galactic Hemisphere can be explained with a combined thermal and cosmic-ray driven wind.

since the source density of supernovae remnants seems to increase with decreasing R , the cosmic-ray source density should increase as well. However, it has been known for some time (e.g. Bloemen 1989) that the inferred cosmic-ray source density is relatively flat, compared to the supernova density, as a function of R .

There has, however, been some debate about whether supernovae remnants are an accurate tracer (since those surveys are subject to various selection effects; see, e.g., Strong et al. 2004, and references therein). Recent surveys of the pulsar population (Lorimer et al. 2006) also show that the pulsar source density increases towards the center of the Galaxy, as shown in Figure 2. This is true irrespective of the model of how n_e varies in the disk, although the magnitude of the pulsar population gradient with R depends strongly on the n_e model. So, there remains a mismatch between the observed source density of cosmic ray “producers” and the cosmic rays themselves.

It has already been pointed out that the observed slow rise in cosmic rays may be due to a wind emerging from the disk, advecting cosmic rays outwards (Bloemen et al. 1993; Breitschwerdt et al. 2002). In the case of Bloemen et al. (1993), a wind model was applied to the entire Galactic disk; as a result, only a very slow wind was found to be compatible with the inferred cosmic-ray source density. In contrast, Breitschwerdt et al. (2002) applied their cosmic-ray and thermally driven wind model, where the wind velocity varied as a function of radius and height; they also took into account anisotropic diffusion. With this model, a small radial gradient in the cosmic ray source density could be explained.

An alternate explanation for this slow change in the cosmic ray population with R was proposed by Strong et al. (2004), who found that a radial variation in the $W_{\text{CO-to-}N(\text{H}_2)}$ ratio by a factor of 5 to 10 could explain the γ -ray observations. In this paper we primarily address the question of the origin of the diffuse, soft X-ray background emission; we will, however, concentrate on a large-scale wind model, keeping in mind its possible application to the cosmic ray source density.

2. A COSMIC RAY AND THERMALLY DRIVEN WIND MODEL

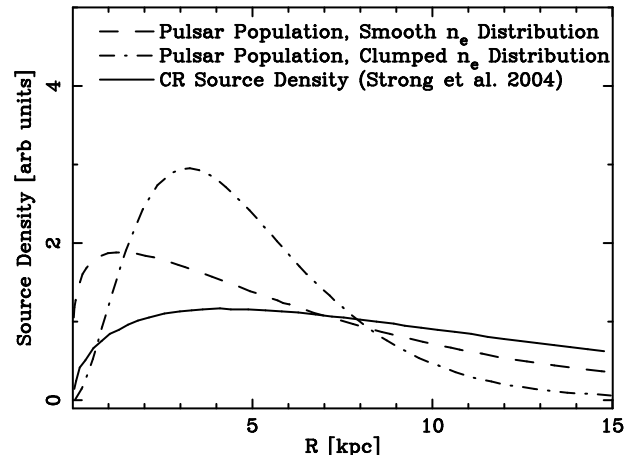


FIG. 2.— Comparison of two different calculations of the pulsar population as a function of Galactocentric radius (Lorimer et al. 2006) vs. the cosmic ray source density implied from the observed γ -ray emissivity (Strong et al. 2004). The two different curves for the pulsar distribution result from assuming a smooth distribution of n_e in the Galaxy (Lyne et al. 1985), or a clumped distribution, using Cordes & Lazio (2002) and Faucher-Giguère & Kaspi (2006); for details, see Lorimer et al. (2006). The fact that the cosmic-ray distribution does not seem to follow the pulsar population has been known for some time (Bloemen 1989), but there is no consensus on the reason. A cosmic-ray and thermal pressure-driven wind may help explain the cosmic-ray source population.

To understand the observations outlined above, we must address both the thermal (soft X-ray) gas and the cosmic ray source density. Therefore, in investigating the possibility of an outflow, we require a Galactic wind model that includes cosmic-ray pressure (exerted via Alfvén waves) and thermal gas pressure. We outline such a model in this section.

Our chief motivation here is to fit the wind model to the observed large-scale soft X-ray emission, and as such, we require a relatively simple model that can be computed quickly to compare with the observations, but one that takes into account the physics of cosmic-ray interactions with the thermal gas. In addition, we are interested in building intuition into the differences between pure thermally-driven winds and

winds with a significant cosmic-ray component (see § 4). We are not the first to address this; a very suitable model has already been developed by Breitschwerdt et al. (1991, hereafter BMV91) and further advanced in later papers (Breitschwerdt et al. 1993; Zirakashvili et al. 1996; Ptuskin et al. 1997; Breitschwerdt & Schmutzler 1999; Breitschwerdt et al. 2002). This work had built on previous analyses of the possibility of cosmic-ray driven winds (Ipavich 1975; Breitschwerdt et al. 1987). In what follows, we explain this 1D, semi-analytic wind model in detail, with particular attention to the differences between our model and that of BMV91.

This 1D model must assume a particular geometric cross-section for the wind; we adopt a flared-cylinder geometry shown in Figure 3, as was adopted in BMV91 and used in studies of coronal holes on the Sun (e.g., Kopp & Holzer 1976). In this geometry, the wind flows along a tube of approximately constant cylindrical cross section up to a height $z \sim z_{\text{break}}$, after which the area increases as z^α :

$$A(z) = A_0 \left[1 + \left(\frac{z}{z_{\text{break}}} \right)^\alpha \right]. \quad (1)$$

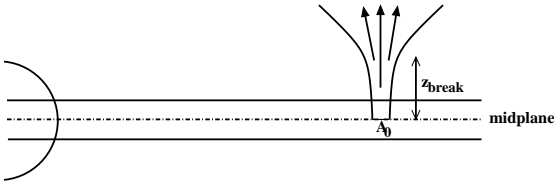


FIG. 3.— The geometry of a flow tube for the 1D wind model. The wind starts at the Galactic midplane with cross-sectional area A_0 , which is roughly constant up to $z \sim z_{\text{break}}$, after which $A \propto z^\alpha$.

We envision that this geometry is set by approximate pressure confinement in the plane of the galaxy up to z_{break} ; above that height, the area diverges spherically (thus $\alpha = 2$). Unlike BMV91, we allow z_{break} to change to find the best-fit wind model. We do not ‘freeze’ this parameter, as we have no *a priori* value for z_{break} for this particular wind geometry (which, in contrast to BMV91, covers only a part of the Galactic disk, and so does not require a scale-height comparable to the scale-length of the star-formation disk for an approximately spherical geometry, for instance). Thus, z_{break} is a fit parameter for our model, in the context of the simplified geometry that we are assuming. Also unlike BMV91, we assume that the wind is launched from the Galactic midplane; this will be addressed in detail when the interaction of cosmic rays, magnetic fields, and thermal gas is discussed, below.

With this geometry, and assuming no additional mass loading of the outflow, the wind has a simple equation of mass conservation:

$$\frac{d}{dz}(\rho v A) = 0, \quad (2)$$

where z is the height above the Galactic midplane, ρ is the density in the wind and v is the wind velocity.

Next, how is the wind driven along this flow tube? We wish to consider the possibility that cosmic-ray pressure, Alfvén wave pressure, and thermal pressure are all important components in driving a Galactic wind. At first glance, this may not seem productive, as cosmic rays seldom interact directly with any particle in the galaxy: the probability of any cosmic ray particle colliding with matter in the Galaxy in

their lifetime is of order 10^{-4} (see, e.g., Kulsrud 2005). However, cosmic rays are observed to have a very small anisotropy (about 1 part in 10^4), which seems at odds with this low collision rate. This small anisotropy is explained by pitch-angle scattering of cosmic rays by Alfvén waves in the ISM. It has been shown that the cosmic rays which supply most of the pressure ($E \lesssim 100$ GeV) can generate these waves via the ‘streaming instability’ (e.g., Wentzel 1968; Kulsrud & Pearce 1969; Kulsrud & Cesarsky 1971). This instability amplifies waves with wavelength of order the cosmic ray gyroradius when the bulk velocity of cosmic rays along the fieldlines exceeds the local Alfvén speed. If the cosmic ray mean free path is much shorter than global lengthscales in the problem, the cosmic rays can be described as a fluid which moves down its pressure gradient at velocity v_A relative to the thermal gas, while transferring momentum and energy to the waves, which in turn transmits them to the thermal gas (e.g., Skilling 1975; Drury & Völk 1981; McKenzie & Webb 1984). We adopt that picture here.

In computing the interaction of cosmic rays, Alfvén waves, and thermal gas, we treat the cosmic rays as an ultra-relativistic polytropic gas with $\gamma_c = 4/3$. (This is an approximation, as γ_c is not exactly $4/3$; see Ensslin et al., 2006.) Meanwhile, we treat the thermal gas as having a polytropic index, γ_g , of $5/3$. Much as in BMV91, we derive equations for the change in gas and cosmic-ray pressure with height in the wind:

$$\frac{dP_g}{dz} = \left(c_g^2 - \gamma_c(\gamma_g - 1) \frac{P_c}{\rho} \frac{1}{M_A} \frac{M_A + \frac{1}{2}}{M_A + 1} \right) \frac{d\rho}{dz}, \quad (3)$$

$$\text{and } \frac{dP_c}{dz} = \frac{\gamma_c P_c}{\rho} \frac{M_A + \frac{1}{2}}{M_A + 1} \frac{d\rho}{dz}, \quad (4)$$

where P_g and P_c represents the gas and cosmic-ray pressure, c_g gives the sound speed in the gas, and $M_A = v/v_A$ is the Alfvén Mach number for the wind. In the gas pressure equation, Equation 3, the first term in parentheses simply relates the change in gas pressure to the change in density as the gas accelerates and expands in the flow tube.

The second term in the parenthesis of Equation 3 represents the coupling of cosmic-ray generated Alfvén waves to the gas; that term gives the heat input to the gas from the damping of those cosmic-ray generated waves. These waves represent the dominant coupling between the cosmic rays and the thermal gas; this process heats the gas despite the drop in density with height (hence the negative sign for this term). As the cosmic-ray generated Alfvén waves are immediately damped, they do not add to the wave pressure, and hence we do not follow their evolution. In our models, the wave pressure at the base of the wind is set to zero, reflecting the small wave energy density in the Galactic plane ($\delta B/B \sim 10^{-3}$ from Kulsrud & Pearce, 1969, where δB represents the Alfvén wave perturbation to the large-scale magnetic field, B). Any energy transferred from the cosmic rays to the waves is immediately input to the gas, as in Equation 3 above. The inclusion of this immediate wave damping in all of the models presented here is an important difference between this work and most of the models in BMV91; we also note that wave damping was considered in much more detail in the later papers of Zirakashvili et al. (1996) and Ptuskin et al. (1997).

This immediate damping of the cosmic-ray generated Alfvén waves is important for two reasons. First, left unchecked the wave pressure can easily grow to such magnitudes that the ratio of the perturbed magnetic field to the

large-scale magnetic field, $\delta B/B$, exceeds unity. In this limit, the derivation of the above equations becomes suspect, as the system becomes nonlinear.

The second objection to unlimited Alfvén wave growth is the presence of rapid damping mechanisms in the ISM. In particular, non-linear Landau damping (Kulsrud 2005) will quickly remove energy from the waves. The rate of non-linear Landau damping is of order

$$\gamma_{\text{NL}} = \frac{\sqrt{\pi}}{4} \sqrt{\beta} \frac{\delta B v_A \Omega}{B v_i} \sim \frac{1}{4} \sqrt{\frac{\pi}{2}} \left(\frac{\delta B}{B} \right)^2 \Omega_i \quad (5)$$

where β is the ratio of the gas pressure to magnetic pressure, $(8\pi P_g)/B^2$, Ω_i is the ion cyclotron frequency, and v_i is the ion thermal velocity. For typical values for our wind models at $z \sim 2$ kpc, ($B = 7.2 \mu\text{G}$, $\delta B/B \sim 10^{-3}$), we find $\gamma_{\text{NL}} \sim 2 \times 10^{-8} \text{ s}^{-1}$, or $\tau_{\text{NL}} \sim 5 \times 10^7 \text{ sec} = 1.6 \text{ yr}$. We can compare this to the advection timescale, $1/((v + v_A) \cdot \nabla P_c/P_c)$, which for a typical wind model is of order 10^{14} s , or $4.3 \times 10^6 \text{ years}$. From this comparison, we can see that the damping is local, since the timescale for non-linear Landau damping is much smaller than the advection timescale. Therefore, the local damping not only allows the quasilinear equations to be applicable throughout the wind, but is physically quite plausible, given the above small damping timescale.

(We note that these arguments were well-known to BMV91, but that the wind models calculated there did not develop large $\delta B/B$ inside the critical point, so such immediate damping was not important in those models [Breitschwerdt 2007, personal communication].)

We briefly consider the effect of Alfvén waves generated by other sources. Cosmic ray streaming is only one source of MHD turbulence in the ISM, and, at large scales, by no means the dominant one. If the turbulence which couples the cosmic rays to the gas were not primarily due to the streaming instability, the model would be substantially modified. The Alfvén speed which appears in the model should be thought of as the mean velocity of the waves in the rest frame of the thermal gas; if the waves were isotropic, this speed would be zero. The cosmic rays would simply behave as a polytropic fluid with adiabatic index γ_c and there would be no frictional heating of the thermal gas. This is not a significant issue, however, because of the anisotropy in the turbulent cascade seen in both experiments and theoretical studies of MHD turbulence (see, e.g. Shebalin et al. 1983; Goldreich & Sridhar 1995; Cho & Vishniac 2000; Milano et al. 2001), which has also been invoked in studies of turbulence in supernovae as well (Ptuskin & Zirakashvili 2003). The turbulence is initially presumably excited at scales of several parsecs or more, far above the cosmic ray gyroradius scale of 10^{12} - 10^{13} cm , and cascades down to the gyroradius scale through nonlinear wave-wave interactions. In order to interact, these waves must be oppositely directed along the magnetic field. By momentum and energy conservation, interactions between such oppositely-moving waves yields resultant waves in which the component of momentum along the magnetic field line has not increased. However, the perpendicular component can increase as a result of the interaction, yielding an anisotropy in \mathbf{k} -space (Shebalin et al. 1983). Thus, at wavenumbers much greater than the driving scale, the perpendicular wavenumber k_\perp much exceeds k_\parallel (Goldreich & Sridhar 1995; Cho & Vishniac 2000). More intuitively, for motions on smaller scales and commensurately smaller energies, the turbulent motions cannot bend magnetic field lines, and the energy is transferred

to motions parallel to the magnetic field, resulting in elongated eddies (Shebalin et al. 1983; Lazarian 2006).

So how does such an anisotropic eddy affect cosmic ray scattering? When $k_\perp/k_\parallel \gg 1$, cosmic rays scatter much less efficiently; this is because, when $k_\perp \gg k_\parallel$, individual cosmic rays sample many uncorrelated perturbations in k_\perp in each gyro-period that effectively cancel out (Chandran 2000; Lazarian 2006). Thus, the background Galactic turbulent cascade has little effect on the cosmic rays compared to the waves they generate themselves. We note, however, that fast-mode waves in the ISM may perhaps be important in scattering cosmic rays (Yan & Lazarian 2003, 2005). For this work, however, we retain the model of quickly damped, cosmic-ray generated Alfvén waves in Equation 3.

Given the importance of gas heating, one may wonder if perhaps a loss term, such as radiative cooling, is also important. We have determined that the radiative cooling is $\sim 1\%$ of the total power in the wind, and so is unimportant for the wind models presented here. However, we note that for very low velocity winds, the dynamical timescale may exceed the radiative cooling time, resulting in significant cooling.

We also ignore cosmic ray diffusion and thermal conductivity. Diffusion is important towards the base of the wind (Breitschwerdt et al. 1993); thermal conductivity may be important there as well: our calculations show conductivity to be important for $z \lesssim 350 \text{ pc}$ in the wind (below that height, the energy input from conduction dominates adiabatic cooling and heating via wave-damping). This is certainly significant, and both effects need to be considered in a more detailed wind model (see §5).

Given Equations 2 to 4, and our assumptions about the coupling of cosmic rays and thermal gas, the above pressure relations are then coupled together in the wind equation, which in its simplest form is

$$\rho v \frac{dv}{dz} + c_*^2 \frac{d\rho}{dz} = -\rho g, \quad (6)$$

where c_* , the “composite sound speed” (see BMV91), is given by

$$c_*^2 = \frac{d(P_g + P_c)}{d\rho} \quad (7)$$

and where the gravitational acceleration, g , is defined by a three-component (bulge, disk, and halo) model given in BMV91. We have compared this gravitational potential model to the more recent work of Dehnen & Binney (1998), and found that, for $z > 200 \text{ pc}$, this newer model gives a lower gravitational acceleration (by $\sim 10\%$ to at most $\sim 60\%$) than the simple model of BMV91; closer to the disk, the model of Dehnen & Binney (1998) yields a higher gravitational acceleration by $\sim 40\%$. With the reduced calculational requirements of the simpler potential (especially important near the critical point of the wind), and the knowledge that the simpler model largely over-estimates the gravitation potential where the wind is accelerating, we choose the simpler model as a conservative approximation; using the more realistic potential, launching a wind from the Milky Way should be somewhat easier than shown here.

We solve the wind equation (Eq. 6) in the 1D flow tube defined by the area law (Eq. 1). While integrating, we use the simple magnetic flux conservation law, $d(BA)/dz = 0$. The integration is carried out using the `dlsode` routine in ODEPACK (Hindmarsh 1983).

TABLE 1
INITIAL (MIDPLANE) WIND PARAMETERS AT
 $R = 3.5 \text{ kpc}$

Parameter	Value	Fixed?
R_0 Range [Galactocentric]	1.5 to 4.5 kpc	Fixed
z_0	1 pc	Fixed
n_0	$1.8 \times 10^{-2} \text{ cm}^{-3}$	Varied
$P_{g,0}/k_B$	$2.6 \times 10^4 \text{ K cm}^{-3}$	Varied
$P_{c,0}/k_B$	$2.2 \times 10^4 \text{ K cm}^{-3}$	Fixed
B_0	$7.8 \mu\text{G}$	Fixed
z_{break}	4.5 kpc	Varied
α	2.0	Fixed

2.1. Initial Conditions

The integrations require that P_g , P_c , ρ , R , and B all be specified at the base of the wind. The value of v is not given at the base of the wind, as its value is set by requiring that the integration pass through the critical point (see § 2.2). Fiducial values for these parameters are given in Table 1, and discussed in more detail below.

The Galactocentric launching radius is set by the observed geometry of the diffuse X-ray emission. If the X-ray emission is roughly centered on Sgr A* (Almy et al. 2000), the extent of the emission out to longitudes of $\sim 30^\circ$ implies a scale for the outer edge of the wind at $R \sim 4.5 \text{ kpc}$ (assuming that the Sun is located at $\sim 8 \text{ kpc}$). The inner edge of the wind is set by the difficulty in launching from the central Galactic potential; for ISM-like launching conditions, we have found that models with $R \lesssim 1.5 \text{ kpc}$ cannot escape the Galaxy. Thus, we set the geometry of our wind to be a “thick curtain”, launched over Galactocentric radii of 1.5 to 4.5 kpc. To run a fiducial model, we set the wind flowtube at 3.5 kpc. More complicated simulations (where separate winds are launched over the complete range or radii) have been run, and show differences in X-ray emission of only $\sim 10\%$. Therefore, the wind models here are simply run at $R \sim 3.5 \text{ kpc}$, and that wind is then applied (or “replicated”) to the range of wind radii (1.5 to 4.5 kpc) and over 2π in azimuth, to fit the observed diffuse X-ray emission. This geometry is shown in Figure 4, below.

This is, of course, a simplification, but one that allows quick calculations of the wind’s X-ray emission and comparison to observations (§ 3), and allows surveys of large areas of parameter space for building physical intuition (§ 4) about galactic winds. It is important to note that, of course, at high latitudes (where $z \gtrsim z_{\text{break}}$), each tube flares outward; with such tubes placed next to each other, they will strongly overlap for $z \gtrsim z_{\text{break}}$. This could be a potential problem, but as we will see later (in §3.4), the X-ray emission is explained with z_{break} being more than a factor of two larger than the emission scale-height, so this will not impact our predictions of the X-ray emission. It would, however, be important for observational tests at higher latitudes.

We must also choose the initial height from which to launch the wind. Again, we differ from BMV91, and choose to launch the wind from the midplane of the Galaxy, with $z_0 = 1 \text{ pc}$. BMV91 choose to launch from $z_0 = 1 \text{ kpc}$ due to concerns about (1) ion-neutral friction due to partially neutral gas for $z < 1 \text{ kpc}$, and (2) an isotropic Alfvén wave field (not generated by the streaming instability of the cosmic rays). While those are all important considerations for the generic ISM, we hypothesize that the hot, ionized medium from which these winds are launched is largely free of neutrals, is dominated by heating and cosmic rays due to nearby supernovae, and that

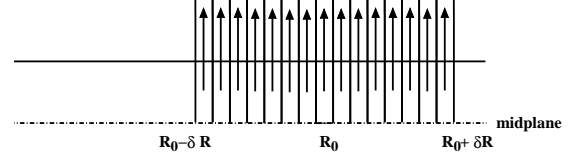


FIG. 4.— Near the Galactic midplane, the flowtubes are vertical, allowing the tubes to be assembled in a simple, large-scale wind model. In this way, our 1D wind models are assembled into a large-scale wind to compare to the observed diffuse soft X-ray emission.

cosmic-ray generated waves dominate the scattering process (see §2). Also, for meaningful comparison with observations, we must model the wind below $z \sim 1 \text{ kpc}$, as the scale height of the diffuse soft X-ray emission is $z \sim 2 \text{ kpc}$ (Snowden et al. 1997).

In order to fit the wind models to the observed diffuse Galactic X-ray emission, the variables P_g , ρ , and z_{break} will be left to “float” (hence allowing the temperature and emissivity of the gas the possibility of matching the observations). But for comparison, it is helpful to consider what prior observational constraints we can place on these values. Unfortunately, it is difficult to constrain the thermal pressure of the hot ionized component of the ISM at $R = 3.5 \text{ kpc}$, or indeed, anywhere in the Galactic disk (see Cox 2005, for a summary). We estimate that at the Sun’s position in the Galaxy, $P_{g,0}/k_B \sim 7000 \text{ cm}^{-3} \text{ K}$ (Cox 2005, in his §4.2). This wind is launched much closer to the Galactic center, so that value must be extrapolated to $R = 3.5 \text{ kpc}$. Wolfire et al. (2003) show that the radial pressure scale-length is of order 5.5 kpc (notably, for the neutral gas component), so to estimate $P_{g,0}(R = 3.5 \text{ kpc})$, we must multiply $P_{g,0}/k_B$ by e^1 . Therefore, $P_{g,0}/k_B \sim 1.9 \times 10^4 \text{ cm}^{-3} \text{ K}$, or $P_{g,0} \sim 2.6 \times 10^{-12} \text{ dyne cm}^{-2}$.

Estimates for the gas density are also difficult for $R \sim 3.5 \text{ kpc}$, but for a simple estimate, if we take $T \sim 10^6 \text{ K}$ for the hot ionized medium (that this wind would be launched from), and use the above pressure estimate, we find $n_0 \sim 1.8 \times 10^{-2}$, or $\rho \sim 1.9 \times 10^{-26} \text{ g cm}^{-3}$.

The cosmic-ray density can be estimated from the synchrotron emissivity; much of the work for this has already been collected by Ferrière (2001). We used her Equations 10 and 11, first duplicating her Figure 7 to check our own implementation; we then use those verified equations to calculate both P_c and P_{magnetic} (and hence B). We find $P_c(R = 3.5 \text{ kpc}, z = 0) = 3.1 \times 10^{-12} \text{ dyne cm}^{-2}$ ($= 2.2 \times 10^4 \text{ cm}^{-3} \text{ K}$). Similarly, $P_{\text{magnetic}} = 2.4 \times 10^{-12} \text{ dyne cm}^{-2}$ ($= 1.7 \times 10^4 \text{ cm}^{-3} \text{ K}$), which implies $B = 7.8 \mu\text{G}$.

We start with $\alpha = 2$ (as in BMV91), but with $z_{\text{break}} = 4.5 \text{ kpc}$, as many of our early wind models preferred z_{break} of that order, as opposed to $z_{\text{break}} = 15$ in BMV91.

2.2. Integrating Through the Critical Point

Like many other similar wind models, this wind equation contains a critical point (CP) where $v = c_*$. Such critical-point equations are usually solved by integrating from the singular point to the boundaries (here at $z = 1 \text{ pc}$ and $z = 1 \text{ Mpc}$). The dependence of the wind on cosmic-ray pressure and gas pressure mean that, in order to follow this usual procedure, estimates of those pressures would have to be known *a priori* at the critical point position. We choose (as did BMV91) to estimate the pressures at the launching point of the wind, searching for a v_0 which defines the wind that threads the crit-

ical point. We checked our implementation by recalculating models presented in Table 1 of BMV91.

This concludes our definition of the cosmic-ray and thermally driven wind model that we will compare to the soft X-ray data. The next section therefore returns to the X-ray data briefly mentioned in §1 and reports on our search for a wind model to fit those observations.

3. COMPARING THE MODEL TO *ROSAT* OBSERVATIONS

One of the main goals of this work is to investigate whether a wind model can reproduce the diffuse soft X-ray background observations most recently presented in Snowden et al. (1997). In this section, we describe the algorithm we developed to calculate that emission.

3.1. Calculating the Average Observed X-ray Emission

We will compare the models against the longitude-averaged X-ray emission as a function of latitude. We retrieved the diffuse X-ray emission maps from <http://www.xray.mpe.mpg.de/rosat/survey/sxrb/12/fits.html> at the “X-Ray Astronomy” page at the Max-Planck-Institut für extraterrestrische Physik. These maps are the full 12’ resolution maps; the emission maps are then averaged over the longitude range from $-30^\circ < l < +30^\circ$, binned 1° in latitude, and plotted vs latitude for the southern Galactic hemisphere only. The Northern Galactic hemisphere contains other features (such as the North Polar Spur) that make model comparisons there much less clear. Note again that there is a slight asymmetry in the observed X-ray emission towards positive Galactic longitudes (towards the right on Fig. 1); we are not modeling that asymmetry here.

The resultant longitude averaged, observed emission is shown by the diamonds in Figure 5 (for the *ROSAT* R4 band, centered at approximately 0.65 keV) and Figure 6 (for the R5 band, centered at approximately 0.85 keV). Error bars (from the original data files) are given by the vertical lines within the diamond-indicated data-points; those error bars assume only statistical errors in the measured X-ray flux. Systematic uncertainties in the foreground and background components (particularly the stellar contribution) may be larger.

We restrict ourselves to the R4 and R5 bands as the emission in those bands comes primarily from oxygen emission lines; higher energy bands (near 1.5 keV, for instance) may depend more strongly on metallicity, as magnesium and silicon emission lines begin to dominate at those energies. In addition, at higher energies, the contribution from the stellar background becomes much more prominent and that background is not well understood (see §3.3).

3.2. Calculating the Wind’s X-ray Emission

The wind model gives $n(z)$ and $T(z)$ along 1D streamlines. As mentioned in § 2.1, the observed large-scale emission is simulated with this wind model by “replicating” the wind solution both in radius (from 1.5 to 4.5 kpc) and in azimuth (see Fig. 4).

First, to calculate the emissivity per emission measure, the emission codes “ATOMDB” and “APEC” (Smith et al. 2001) were used to generate spectra for a range of temperatures⁵

⁵ As noted on their website (<http://cxc.harvard.edu/atomdb/>), APEC is not complete below about 0.25 keV, but that will not greatly affect the predictions here, since the relevant bands for this work are at higher energies.

from $10^{5.6}$ to $10^{7.6}$ K in steps of $10^{0.1}$ K. These codes use the metallicities of Anders & Grevesse (1989). Each APEC-generated spectrum was then folded through the *ROSAT* response matrix⁶, with the responses of the individual channels summed into groups to represent the *ROSAT* passbands R4 and R5 (Snowden et al. 1995)⁷. Applying these general models to the wind, the resulting matrix of emissivity per emission measure vs temperature for each band is then interpolated to calculate the emissivity at each point in the wind model. We find that the newer APEC-derived models yield a maximum of 50% more emission in the M-band (the combined *ROSAT* R45 band) than the Raymond & Smith (1977)-derived models of Almy et al. (2000) near $T = 4 \times 10^6$ K, but the differences are only of order 20% near $T = 2 \times 10^6$ K.

The emission measure is calculated by simply summing $n_e^2 \Delta l$ along lines-of-sight through the wind model. This model emission is then corrected for absorption by applying (as a foreground absorption screen) the N_H data of Dickey & Lockman (1990) for each line of sight. The resultant wind emission for both the R4 and R5 bands is shown as the dashed line in Figures 5 and 6, respectively.

We note briefly that we have checked that the gas in these winds is in equilibrium throughout the region where X-ray emission is important. This has been verified with the non-equilibrium cooling code of Benjamin et al. (2001). For instance, for the best-fit wind model presented in §3.4, we have found that non-equilibrium calculations yield only 1% differences in the population of fully-ionized oxygen vs. equilibrium at $z = 2$ kpc, whereas for less ionized states of oxygen, non-equilibrium calculations show 1% deviations only beyond $z \sim 4.5$ kpc. Since we are interested in the X-ray emission at $z \lesssim 2$ kpc, we retain simple collisional-equilibrium models. The previous Galactic outflow model of Breitschwerdt & Schmutzler (1999), also of a hybrid cosmic-ray and thermal-gas pressure driven wind, relied on non-equilibrium effects (Breitschwerdt & Schmutzler 1994) to model the full-sky *ROSAT* emission in the all of the observed bands; the present model concentrates solely on the excess towards the Galactic Center, and for reproducing these observations and for this wind model, we find that collisional equilibrium dominates. Non-equilibrium effects may certainly be important at very large heights ($z \sim 20$ kpc) and correspondingly cool temperatures, but we do not find those effects to be significant in reproducing the *ROSAT* R4 & R5 emission.

3.3. Calculating the Background Emission

As first considered by Almy et al. (2000), various background sources also contribute emission to the soft, diffuse X-ray observations. The stellar and extragalactic backgrounds listed below were used in Almy et al. (2000), and were both folded through both the Galactic N_H map and through the *ROSAT* response matrix.

The extragalactic emission is calculated using the power-law given in Hasinger et al. (1993):

⁶ We used a file `pspcc_gain1_256.rsp`, downloaded on Feb. 22, 2006 from the “X-ray Background Tool” on the HEASARC website at <http://heasarc.gsfc.nasa.gov/docs/tools.html>

⁷ NB: We found that the channel boundaries reported in Snowden et al. (1995), when used to sum up the channel-by-channel responses to create the R4 and R5 band responses, *did not* recreate the response matrices plotted in Snowden et al. (1997) and Almy et al. (2000). The only way to reproduce the previous response matrices was to subtract 6 channels from the channel boundaries in Snowden et al. (1997). In order to compare the wind model to the data, it is essential that we use as similar a response matrix as possible to that used in Snowden et al. (1997), so we apply this channel offset.

$7.8 (E/1\text{keV})^{0.96} \text{ keV cm}^{-2} \text{ s}^{-1} \text{ sr}^{-1} \text{ keV}^{-1}$ for $E < 1 \text{ keV}$. This averaged extragalactic background is shown as the dot-dot-dot-dashed line in Figures 5 and 6.

The stellar background used is the model of Schmitt & Snowden (1990). This background model is shown as the long-dashed line in Figures 5 and 6. There are significant uncertainties with this stellar background model; Kashyap et al. (1992) claim that there are errors of order a factor of three in Schmitt & Snowden (1990) due to the assumed luminosity function; unfortunately, however, Kashyap et al. (1992) do not model the stellar emission towards the Galactic Center. We retain the stellar model of Schmitt & Snowden (1990) because it addresses the stellar background in that area. The uncertainty in this background represents another reason for the present work to not address the 1.5 keV emission, which would be even more strongly contaminated by coronal emission; emission in the R4 and R5 bands is not as strongly affected by the stellar background.

All of the above extragalactic and background emission, added together, do not fully account for emission at high latitudes ($b < -60^\circ$). The wind model emission is also insignificant at this height. To account for this excess emission, we add in an isotropic component (the dotted line in Figs. 5 and 6). This emission may be due to poorly-understood disk and halo emission that provides a rather uniform and apparently thermal-emission background at high latitudes and towards the Galactic anticenter. This component is simply fitted (for each model fit to the data) to account for the emission in the latitude range $-90^\circ < b < -60^\circ$.

3.3.1. Refitting the Static Polytrope Model

The best-fit wind model will be found by comparison with the observations, below (§3.4), but it is also instructive to compare the wind model to the static polytrope model of Almy et al. (2000). Having updated several steps in the data and model analysis procedures, we re-fit the polytrope model to the data to ensure that both models are given fair consideration. We therefore adapted the wind-model routines and parameter-search codes to produce new polytrope models and find the best polytrope fit, again using $\gamma = 5/3$ as in Almy et al. (2000). We produced a grid of 101×101 polytrope models, stepping logarithmically between P_0/k_B from 1.8×10^4 to $1.8 \times 10^6 \text{ cm}^{-3} \text{ K}$ and through k values of 1.45×10^{31} to $1.45 \times 10^{33} \text{ cm}^4 \text{ g}^{-2/3} \text{ s}^{-2}$. This parameter survey confirmed that the Almy et al. (2000) values for those polytrope constants remains the best-fit: we find $P_0/k_B = 1.8 \times 10^5 \text{ cm}^{-3} \text{ K}$ and $k = 1.45 \times 10^{32} \text{ cm}^4 \text{ g}^{-2/3} \text{ s}^{-2}$. This model, added to the background sources already considered, yields the polytrope models shown by the dot-dashed lines in Figures 5 and 6.

3.4. Fitting the Wind to the Observed Emission

The longitude-averaged wind model's X-ray emission is added to the various background components, and the sum is given as the solid black line in Figures 5 and 6. For each attempted model fit (see below), χ^2 is calculated by considering the full range of latitudes plotted, weighted by the errors shown in the data points. The reduced χ^2 values are not close to unity, but we retain χ^2 as a relative figure-of-merit for comparing a wide range of models.

To find the best-fit model, an initial parameter survey was carried out over two orders of magnitude in ρ_0 and $P_{g,0}$ (centered near the initial parameters given in Table 1), and a factor of 4 in z_{break} ; the parameter ranges of ρ_0 and $P_{g,0}$ were grid-

TABLE 2
"BEST-FIT" WIND PARAMETERS

Parameter	Value	Fixed?
$P_{g,0}/k_B$	$2.0 \times 10^4 \text{ K cm}^{-3}$	Varied
n_0	$6.9 \times 10^{-3} \text{ cm}^{-3}$	Varied
z_{break}	5.2 kpc	Varied
R_0 Range [Galactocentric]	1.5 to 4.5 kpc	Fixed
$P_{c,0}/k_B$	$2.2 \times 10^4 \text{ K cm}^{-3}$	Fixed
B_0	7.8 μG	Fixed
α	2.0	Fixed

ded into 35 steps; while z_{break} was gridded into 5 bins. After this more general survey found the approximate location of the best-fit model, higher resolution sampling was carried out, leading to steps of $\sim 1.3\%$ in ρ_0 and $P_{g,0}$, and $\sim 6\%$ steps in z_{break} near the χ^2 minimum. The best fit model parameters are given in Table 2 with X-ray emission shown in bands R4 and R5 in Figures 5 and 6, respectively. The best-fit model's position in χ^2 space is fairly well constrained, as shown by the green ellipse in Fig. 10. Notably, at fixed z_{break} , the fits for the individual *ROSAT* emission bands are very close together; the best-fit R5 model is identical to the joint best-fit R4 & R5 model, and the best-fit R4 model differs by only 9% in $P_{g,0}$.

Interestingly, the $P_{g,0}$ value obtained is quite similar to the ISM value that was initially estimated. Granted, our initial, pre-fit estimate of $P_{g,0}$ (in Table 1) could have uncertainties of at least a factor of two, but it is somewhat satisfying that the wind's required pressure is relatively close to the nominal ISM thermal pressure at the launch position. Meanwhile, the density at the base of the wind is 1/3 of our estimate of the ISM density.

It is important to note also that $P_{c,0} \sim P_{g,0}$, and so in this best-fit model, *cosmic rays are an important component in driving a wind from the Milky Way*. In fact, in the best-fit wind model, $P_{c,0}$ is very slightly greater than $P_{g,0}$ (but only by 10%). Of course, our value of $P_{c,0}$ is set from synchrotron measurements (Ferrière 2001): the diffuse X-ray emission by itself can place only fairly weak constraints on the cosmic-ray pressure, and only then because the damping of cosmic-ray generated waves increases the temperature of the gas slightly (in the best-fit model, $T_{\text{max}} \sim 1.15T_0$), or leads to a wind that cannot escape the Milky Way. Judging from an increase of χ^2 by $\sim 50\%$, the X-ray data constrains $P_{c,0}$ to lie between $\sim 10^4 \text{ cm}^{-3} \text{ K}$ and $\sim 6 \times 10^4 \text{ cm}^{-3} \text{ K}$. (For n_0 constant, the best fit $P_{c,0}$ is $2.7 \times 10^4 \text{ cm}^{-3} \text{ K}$, only $\sim 20\%$ away from our assumed $P_{c,0}$.)

The parameter z_{break} is also important to fitting the *ROSAT* data. Moving z_{break} directly impacts the location of the critical point, and therefore the fall-off of X-ray intensity with height. Having no *a priori* constraint for the value for z_{break} for this geometry, we allowed the parameter to float, finding the best fit value of $z_{\text{break}} = 5.2 \text{ kpc}$. Again, judging from an increase in the minimum χ^2 by $\sim 50\%$, z_{break} is approximately constrained to lie between 4.1 kpc and 6.5 kpc. To help guide intuition: as z_{break} decreases, the critical point position decreases, the mass outflow rate increases, and the total energy required increases.

The comparison between the wind model, static polytrope model, and data shows that the wind is an improved fit to the data. The χ^2 values for bands R4 and R5 are smaller by a factor of 2.1 and 2.3 for the wind models compared to the static polytrope model. The χ^2 values are themselves very

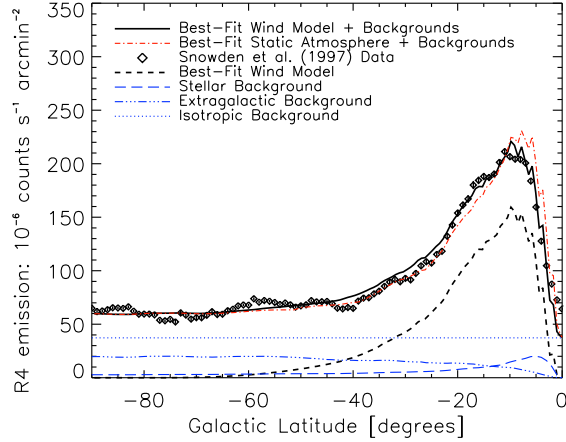


FIG. 5.— *ROSAT* R4-band emission (centered on ~ 0.65 keV) from the best fit wind model (Table 2) compared to the longitude-averaged diffuse X-ray emission from Snowden et al. (1997). The *ROSAT* data points are plotted as diamonds, with vertical lines representing the error bars; the error bars are of very similar size to the plotting symbols. In the R4 band, the wind and static-polytrope models both fit the data reasonably well, although the χ^2 for the wind is 2.1 times smaller than that for the static-polytrope. Still, systematic deviations dominate: $\chi^2_\nu = 19.0$ for the best-fit wind model in the R4 band.

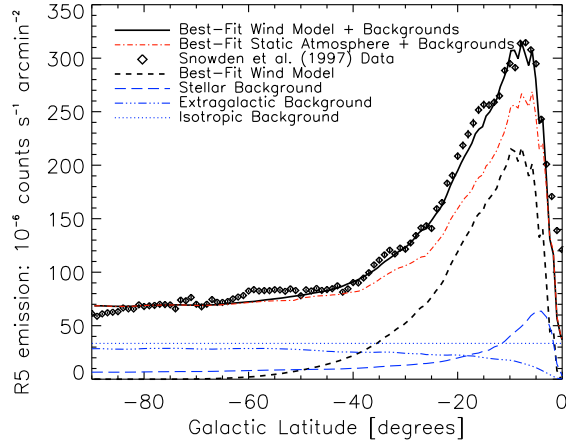


FIG. 6.— *ROSAT* R5-band emission (centered on ~ 0.85 keV) from the best fit wind model (Table 2) compared to the longitude-averaged diffuse X-ray emission from Snowden et al. (1997). The *ROSAT* data points are plotted as diamonds, with vertical lines representing the error bars; the error bars are of very similar size to the plotting symbols. In the R5 band, the wind models fits much better than the static-polytrope model, with a difference of 2.3 in χ^2 . As for band R4, χ^2_ν is not near unity, with a value of 48.9; again, systematic deviations from the model dominate.

high ($\sim 5.9 \times 10^3$ for the best fit model), showing that there are still many deviations between the data and wind model, but an examination of Figures 5 and 6 show that this simple wind model is at least a reasonable fit to the data, and therefore merits continued detailed consideration.

3.5. The Best-Fit Wind Model

Before moving on to consider the range of models produced in our parameter surveys, it will help to consider the best-fit model in some detail. In Figure 7, we show the trends in velocity vs height for the best-fit wind model. The solid

line represents the velocity curve for outflowing gas in the wind; like all thermal winds, it starts at an initial velocity less than the sound speed, accelerates through the critical point (where $v = c_*$) and asymptotes at a velocity of order the escape velocity. Interestingly, in this model, the position of the critical point is $z_{CP} = 2.4$ kpc, near the edge of the region of observed emission. Also, this wind requires an initial velocity of $v_0 = 173$ km s $^{-1}$; in comparison, at the base of the wind, $c_{s,0} = 198$ km s $^{-1}$ (from $T_0 = 2.9 \times 10^6$ K) while $c_{*,0} = 251$ km s $^{-1}$. The terminal velocity of the wind is $v_\infty \sim 760$ km s $^{-1}$.

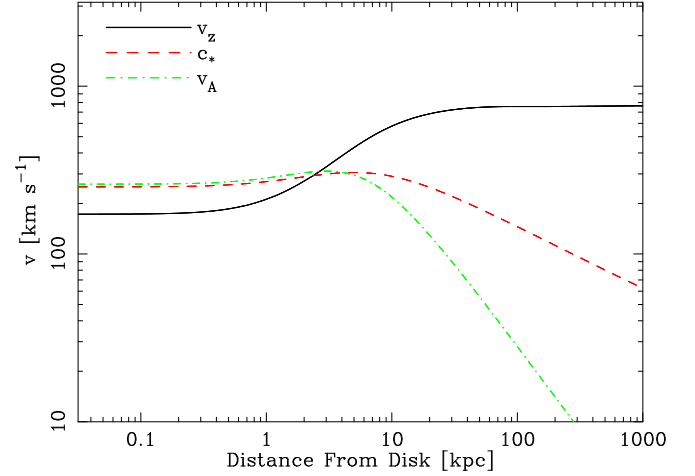


FIG. 7.— Velocity vs. height in a fiducial wind model. The solid line represents the wind velocity, the dashed line represents c_* , the composite sound velocity, and the dot-dashed line shows the change in the Alfvén velocity with height. This velocity curve shows the rather standard increase in velocity of a pressure-driven wind, rising from the relatively low v_0 , through the critical point at $v = c_*$, and accelerating on to $v \sim v_\infty$.

Figure 8 shows how the gas and cosmic-ray pressures compare, and how they each change with height in the wind. The cosmic-ray pressure and gas pressure are nearly equal at the base of the wind, but at large scales the cosmic-ray pressure drops off less quickly than thermal pressure, as we have assumed that $\gamma_c = 4/3$ and $\gamma_g = 5/3$ (for cosmic rays and gas, respectively). The large-scale importance of cosmic rays will be investigated further, below.

We present the changes in density and temperature with height in Figure 9. The temperature shows an increase at around $z \sim 2-3$ kpc due to the damping of the cosmic-ray generated waves. The density simply falls off with height as expected from mass conservation; the density drops off so quickly that the increase in temperature due to wave damping does not yield an increase in gas pressure at large height, although the gas pressure does drop off more slowly with height than it would in the absence of cosmic-ray wave damping.

The importance of this wind for the Galaxy is largely summed up in the mass outflow rate: for this model, $\dot{M} = 2.1 M_\odot$ yr $^{-1}$. This is a very large mass outflow rate, but is in the same range as the inferred mass inflow rate to the Galaxy of $\sim 1-10 M_\odot$ yr $^{-1}$ (Bregman 1999). Even with that infalling gas, this wind would have important implications for metallicity gradients in the Milky Way. However, we note that while that mass outflow rate is well-constrained within the context of this simple model, there are factors which we do not con-

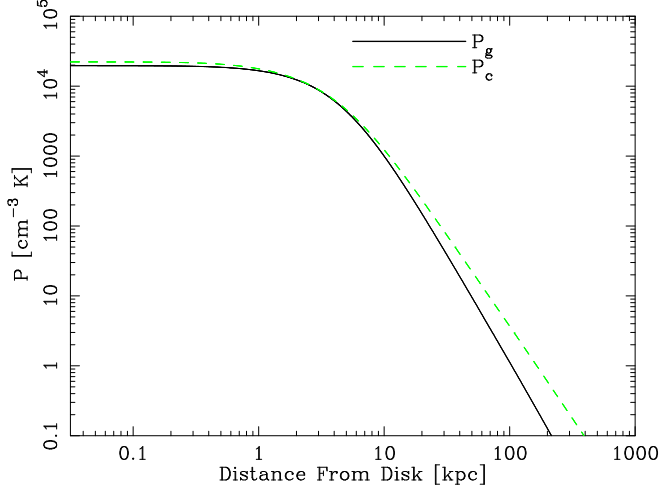


FIG. 8.— Pressure vs. height in a fiducial wind model. The solid line shows the thermal pressure and the dashed line shows the cosmic-ray pressure. Because $\gamma_c = 4/3$ and $\gamma_g = 5/3$ in our model, the cosmic-ray pressure drops off more slowly with height in the wind. In addition, as cosmic-ray driving is somewhat less efficient than thermal driving (see §4.3), the thermal pressure is most significant at the base of the wind, whereas the cosmic-ray pressure is most significant at large (kpc) heights.

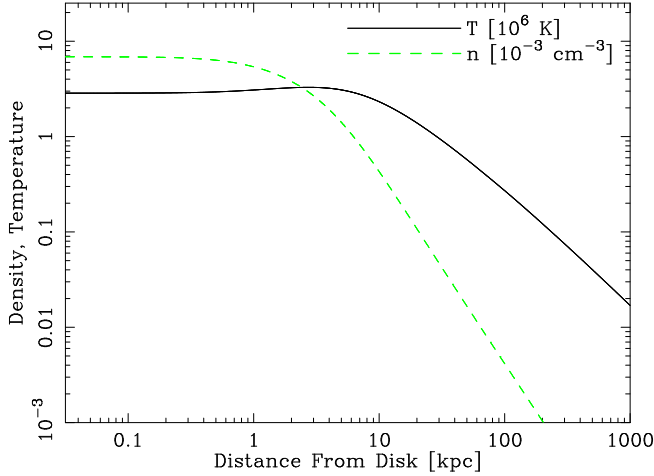


FIG. 9.— Normalized density and temperature vs. height in a fiducial wind model. The temperature is normalized to 10^6 K and the density is normalized to 10^{-3} cm^{-3} . The temperature briefly increases to a peak at $z \sim 3$ kpc because of the damping of cosmic-ray derived Alfvén waves. The density, however, drops off quickly enough with height that the gas pressure remains monotonic (see Fig. 8), as it must for the wind to be driven to large heights.

sider which may significantly decrease the required mass outflow rate. For instance, clumping in the wind (see §5) could lower the mass outflow rate required to supply the observed emission; the “best-fit” wind here (with constant density at the base) would therefore represent a maximal mass-loss wind.

3.6. Why Does the Wind Fit Better than a Static Atmosphere?

Overall, one might expect the wind shown here to yield emission similar to a static atmosphere, as the outflow is close to hydrostatic equilibrium within the critical point. This is true, but there is one principal reason why the wind improves

upon the previous static atmosphere models. The wind is defined to lie between 1.5 and 4.5 kpc: the outer radial bound does not affect the difference of fit (since the longitude range of the survey data used here is limited anyway), but the inner bound is important, and is physically motivated: the Galactic potential there makes launching a wind unlikely, except under extreme conditions. (There could, of course, still be X-ray emitting gas within the Galactic core representing a fraction of the observed emission; the inclusion of such emission would lower the required mass outflow rate in this outflow.) In contrast to the wind model, the static polytrope must, by definition, fill the core of the Milky Way. This leads to extremely high temperatures (given the deep potential) and overestimates of the emission near the Galactic center in order to have approximately correct emission temperatures elsewhere, although perhaps thermal conduction could compensate for this (Almy et al. 2000).

Also, we note that the drop-off in temperature with distance in the static polytrope model, and the necessity of the central very high-temperature region, means that the temperature elsewhere in the wind is, on average, somewhat smaller than required to explain the emission. This can be seen in Figure 6.

Compared against the static-atmosphere model, then, the wind model is the preferred fit for the diffuse soft X-ray data. But how do such wind models work as the fit parameters are varied? These questions are addressed in the following section.

4. HOW GALACTIC WINDS CHANGE WITH INITIAL PARAMETERS: BUILDING INTUITION

The parameter surveys that yield a best-fit model are also quite useful for building intuition and understanding of mixed cosmic-ray and thermally-driven winds. We present a few of the key results below. For each survey, we have varied the parameters around the best-fit values for the Milky Way to understand how the outflow would change character near the best-fit parameter values.

4.1. Mass Outflow Rate

Figure 10 presents the range of mass outflow rates given in a variety of thermally and cosmic-ray driven wind models. First, it is instructive to consider the envelope of winds that successfully escape the Galaxy’s potential vs. the unshaded area where winds could not be launched. Towards the bottom-right of the plot, at low densities and high pressures, gas is hot enough to escape simply by virtue of $c_{s,0} > v_{\text{esc}}$. These are not outflows that our code models, and so those regions are not filled-in on the contour plots. In fact, if the wind were purely driven by thermal pressure, gas with $T > T_{\text{high}}$ in the plot would “evaporate” in this way.

In the same limit of a thermal-pressure dominated wind, if $T < T_{\text{low}}$, the gas would not have enough energy to escape. Thus, the upper limit of the shaded area in Figure 10 represents winds that are becoming too dense (and thus too cold) to escape the Galactic potential. The “excess” of allowed winds with $T < T_{\text{low}}$ exists because of the added cosmic-ray pressure gradient. The cosmic-ray pressure component acts over larger distances than the thermal-pressure component (as $\gamma_c < \gamma_g$), and helps drive the wind where a thermal wind alone would fail: *cosmic-ray pressure thus markedly increases the parameter space where viable winds may be launched.*

Looking inside the perimeter of the shaded region in Figure 10, we see that, as expected, as we increase the temperature of the gas (increasing $P_{g,0}$ at constant n_0), the mass out-

flow rate increases. Meanwhile, increasing n_0 at constant $P_{g,0}$ decreases the temperature of the gas, yielding less energy to the gas, and so produces smaller mass outflow rates.

In more detail, though, why does Figure 10 show curvature in the contour levels? For any given value of $P_{g,0}$, there are two values of n_0 where a given mass outflow rate can be achieved. To understand this, recall that the \dot{M} contours are basically contours of $n_0 v_0$. The initial velocity, v_0 , decreases as the base temperature decreases. One can think about this as follows: a decrease in temperature yields a decrease in the energy available to the gas at the base of the wind, and drives the mass outflow rate down; so, at some fixed $P_{g,0}$, as the density increases, v_0 must decrease. Since $\dot{M} \propto n_0 v_0$, even as n_0 increases, this decrease in v_0 leads to a decrease in \dot{M} , and produces the curvature in the \dot{M} contours.

Our chosen (fixed) parameters can also affect the available parameter space of escaping winds. For instance, $\alpha \gtrsim 2$ is important for launching a wind; for $\alpha \sim 1.0$ the wind cannot pass through a critical point. Thus, the value of α can also strongly affect where winds are allowed. We retain $\alpha = 2$ as in BMV91.

4.2. Total Energy Flux in the Wind

Of great interest for the production and impact of these winds is their total power (total rate of energy release in both kinetic energy and enthalpy). At the base of the wind, the enthalpy dominates the kinetic power, so the total power simply scales as the base temperature in the wind (although plateauing at low gas pressure because of the added enthalpy in cosmic rays). Approximately 75% (and $\sim 90\%$ for the best-fit model) of the power at the base of the wind is in enthalpy.

We now check whether that power can be supplied by supernovae in the Galaxy. The total power required for the wind is $\sim 3.7 \times 10^{41}$ ergs s^{-1} . To calculate the normal SN power in the Galaxy, we use the SN rates per unit area for both Type I and Type II SN in Ferrière (2001) in her Equations 14 and 16. Integrating over the area of the wind only, we find a SN rate of ~ 5400 Myr $^{-1}$, which equates to roughly 1 SN every 180 yrs. If each SN produces 10^{51} ϵ ergs (where ϵ is the fraction of SN power placed in cosmic rays and thermal gas), then the total SN power in the disk (below the wind only) is $\sim 1.7 \times 10^{41}$ ϵ ergs s^{-1} . This simple estimate therefore shows that the wind requires of order the normal SN rate in the disk, although it is a factor of ~ 2 too high. Of course, we are applying a very simple model, and it is quite conceivable that, by including conduction (which would act as a heat source to add energy to the base of the wind), and by considering the effects of clumping within the wind, the outflow's energy requirements could be reduced (see §5).

4.3. The Importance of Cosmic Rays

Figure 11 plots the mass outflow rate in the wind, as in Figure 10, but as a function of cosmic-ray pressure and gas pressure. The solid black contour lines in the plot show lines of constant total pressure. Thus, moving counter-clockwise along those lines moves from gas-pressure dominated winds to cosmic-ray dominated winds.

Before we consider the effect of cosmic rays in these particular models, we start with some general considerations that will help us later on. First, as has been known for some time, momentum addition either before or after the critical point of a wind affects the outflow differently (e.g. Leer & Holzer 1980; Feldmeier et al. 1999). Momentum input be-

fore the critical point results in an increase in the mass outflow rate, whereas momentum input after the critical point increases the terminal velocity. In the context of these models, the smaller adiabatic index of cosmic rays means that the cosmic-ray pressure decays more slowly (see Fig. 8), and therefore increases in the cosmic-ray pressure tend to increase the terminal velocity as well as the mass outflow rate (although cosmic rays are less efficient at “mass-loading” the wind, or setting the mass outflow rate, than gas pressure, as we will see shortly). On the other hand, increases in the gas pressure tend to increase the mass outflow rate, with relatively minor changes to the terminal velocity unless the gas pressure is dominant. This is an important point to keep in mind as we discuss the role of cosmic rays in these winds.

Now consider the outline of the shaded region in Figure 11: this outline denotes the transition from wind models that pass through a critical point and winds that do not have a critical point, or that fail to launch gas to large heights altogether. Again, at the high thermal pressure limit (and therefore high-temperature limit, near $P_{g,0} \sim 10^5$ cm $^{-3}$ K), the gas is initially too hot and forms a more evaporative flow. At high cosmic-ray pressure towards the top of the map ($P_{c,0} \sim 2 \times 10^5$ cm $^{-3}$ K), we see that cosmic-rays can launch winds even down to fairly low thermal pressures, if the cosmic-ray pressure dominates (more on this below). However, there is an upper limit in cosmic-ray pressure beyond which the mixed cosmic ray and thermal pressure can launch an outflow that does not require passage through a critical point. Beyond this limit, gas of all initial velocities can go to infinity, and no single wind solution is preferred.

4.3.1. The Relative Efficiency of Cosmic-Ray Driving

Looking at the basic structure of colored contour lines in Figure 11, it is clear that generally, as we increase either the gas pressure or the cosmic-ray pressure, the mass outflow rate generally increases. This makes sense since increased pressure leads to increased energy in the gas which can help increase \dot{M} .

But, it is important to note that the colored contour outlines do not exactly follow the contours of total pressure. This is clearly seen at the high-pressure limit, where the outline of the shaded region does not follow the contours of total pressure. This is explained by the relative inefficiency of cosmic-ray pressure vs. gas pressure in driving gas from the Galactic midplane. An intuitive explanation of this comes from understanding that $(v + v_A)\nabla p_c$ is the rate that the cosmic-ray pressure transfers energy to the flow ($v\nabla p_c$ is the rate of work done on the gas moving at v , whereas $v_A\nabla p_c$ is the rate of work done to generate Alfvén waves via the streaming instability). For $M_A \ll 1$, $v \ll v_A$, and this rate is much smaller than downstream in the wind where $v > v_A$. As the low-velocity region is the region of mass-loading, it follows that \dot{M} will drop if the proportion of cosmic-ray pressure increases for some given, constant total pressure. This explains why following one contour of constant pressure (counter-clockwise) from high thermal pressure to high cosmic-ray pressure leads to a drop in mass outflow rate.

In more mathematical detail, we can see the reason for this difference in efficiency by considering the drop in cosmic-ray pressure with density (and therefore drop with height in the wind, Eq. 4) in the sub-Alfvénic and super-Alfvénic regimes:

$$\lim_{M_A \rightarrow 0} \frac{dP_c}{dz} = \frac{\gamma_c P_c}{2\rho} \frac{d\rho}{dz} \quad (8)$$

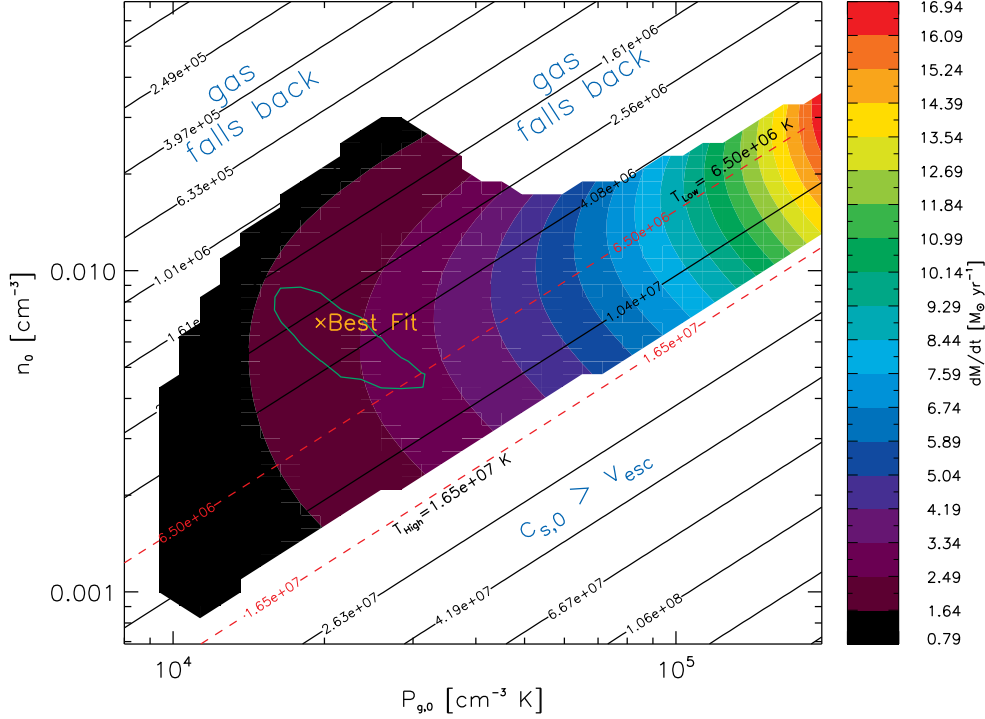


FIG. 10.— Color contours of mass outflow rate in units of $M_{\odot} \text{ yr}^{-1}$, with temperature (in K) represented by solid black contour lines, as a function of base density, n_0 , and gas pressure, $P_{g,0}$. The shaded contour region shows those winds that pass through a critical point, as distinct from those regions where T is too high ($c_{s,0} > v_{\text{esc}}$) and where T is too low, and the gas falls back. These regions of failed wind are approximately defined by either $T \gtrsim T_{\text{high}}$ or $T \lesssim T_{\text{low}}$: the temperature limits for a *pure thermal wind* with our parameters, shown here with the red, dashed-line contours. The excess of viable winds with $T < T_{\text{low}}$ occurs where cosmic-ray pressure helps drive the wind even at low temperatures. The best fit model for both the “R4” and “R5” bands is shown as the gold cross; note that without cosmic-ray pressure, no such wind would be possible from the Milky Way. The area where $\chi^2 < 2 \cdot \chi^2_{\text{min}}$ is shown as the green ellipse. For winds in this survey, R_0 , z_0 , $P_{c,0}$, B_0 , z_{break} , and α (see Table 2) were fixed.

$$\text{and } \lim_{M_A \rightarrow \infty} \frac{dP_c}{dz} = \frac{\gamma_c P_c}{\rho} \frac{d\rho}{dz}. \quad (9)$$

Since we assume $\gamma_g = 5/3$ and $\gamma_c = 4/3$, the factor of 2 in the first equation above only exacerbates the difference between cosmic-ray and thermal driving: γ_c is effectively $2/3$ compared to $\gamma_g = 5/3$ in sub-Alfvénic gas. The ratio of the effective γ factors is 2.5; this will become important in the discussion below. So, in the sub-Alfvénic regime, dP_c/dz drops more slowly than dP_g/dz , which means that less momentum is imparted to the gas; hence, we may conclude that cosmic rays drive gas less efficiently when the wind is sub-Alfvénic. If the winds were everywhere (in Fig. 11) launched sub-Alfvénic, then the cosmic-ray driven winds would require pressures about a factor of 2.5 higher than the thermally-driven winds.

This complication is that, at high $P_{c,0} \sim 10^5 \text{ cm}^{-3} \text{ K}$, the winds are somewhat super-Alfvénic at the base, whereas at lower $P_{c,0}$, the winds are Alfvénic to sub-Alfvénic (Fig. 11 is for fixed n_0 , so the colored contours on this plot are curves of v_0 , which therefore decreases as $P_{c,0}$ decreases). Winds that are launched with super-Alfvénic velocities will have more efficient cosmic-ray driving. So, some of the difference in required launching pressures between cosmic-ray and thermally dominated winds are also due to a transition from sub-Alfvénic to somewhat super-Alfvénic which compensates for the fact that the winds are not strictly launched in the $M_A \ll 1$ or $M_A \gg 1$ regimes.

In understanding the relative efficiency of cosmic-ray driving, we have only explained the basic trends in \dot{M} with total pressure and the high-pressure limit of Figure 11. We

now turn to the low-pressure limit, where winds also cannot emerge from the Galactic midplane.

4.3.2. The Impact of Alfvén Wave Damping

The relative efficiencies of cosmic-ray and thermal pressure driving do not explain the lack of winds at low thermal pressure ($P_{g,0} < 10^4 \text{ cm}^{-3} \text{ K}$) and low to intermediate cosmic-ray pressure ($P_{c,0} < 10^5 \text{ cm}^{-3} \text{ K}$). At the very lowest total pressures ($P_{\text{total}} \lesssim 10^4 \text{ cm}^{-3} \text{ K}$), winds cannot be launched because the pressure is simply too low (cosmic-ray driven winds would be possible for lower initial densities, however). But at higher cosmic-ray pressures, winds cannot be launched because Alfvén wave damping and the resultant heating dominates. For intermediate $P_{c,0}$ and low $P_{g,0}$, the damping of Alfvén waves can actually lead to a large increase in temperature and therefore an *increase* in P_g with height; this pressure increase can cause the wind to stall (BMV91). So, in this regime, the Alfvén wave damping actually “pressurizes” the Galactic disk and *prevents* a wind from being launched from the midplane. We have verified this result by running a parameter survey identical to that shown in Figure 11, but with wave dissipation turned off; as expected, the lack of dissipation allows winds to form with $P_{g,0} < 10^4 \text{ cm}^{-3} \text{ K}$ and with $P_{c,0} < 10^5 \text{ cm}^{-3} \text{ K}$. For winds with higher $P_{c,0}$ and low $P_{g,0}$, the cosmic-ray pressure dominates to such an extent that the wave damping does not hamper wind driving. (Of course, all of these constraints on pressure components are only strictly valid for launching from the Milky Way’s midplane, as we have assumed.)

4.3.3. Launching Winds at Low $P_{c,0}$

We now understand most of Figure 11 except for the small gap in wind models at low cosmic-ray pressure and intermediate gas pressure ($10^4 \text{ cm}^{-3} \text{ K} \lesssim P_{g,0} \lesssim 4 \times 10^4 \text{ cm}^{-3} \text{ K}$, $P_{c,0} \lesssim 5 \times 10^3 \text{ cm}^{-3} \text{ K}$). In this region, the winds are not so strongly dominated by either cosmic-ray pressure or gas pressure, Alfvén wave damping will not be important (because of the relatively low P_c), and the two must operate in concert. The unshaded region defined above is essentially the region where the inequality in the pressures leads to difficulty in self-consistently launching a wind (which gas pressure is especially good at; see above) and driving it to infinity (where cosmic-ray pressure starts to dominate). If the thermal wind attempts to load too much mass at the base of the wind (more than the very low cosmic-ray pressure can handle), the wind fails at large radii. If the thermal wind loads the wind with a fairly low mass outflow rate, the very low cosmic-ray pressure can continue to loft the gas to large distances after the gas pressure decays away. This is corroborated by the very low mass outflow rate associated with the “promontory” of low mass outflow rate near $P_{g,0} = 9 \times 10^3 \text{ cm}^{-3} \text{ K}$ and $P_{c,0} = 2 \times 10^3 \text{ cm}^{-3} \text{ K}$.

5. CONCLUSIONS

We have implemented a simplified cosmic ray- and thermally-driven wind and have used it to try to explain the soft, diffuse X-ray emission seen towards the Galactic Center. We find that such a wind can indeed match the observed averaged X-ray emission quite well, and in fact fits demonstrably better than the static polytrope model of Almy et al. (2000). It is important to note that this wind is approximately equally powered by both cosmic rays and thermal pressure: cosmic rays are important in helping this relatively cool wind escape from the Galactic potential. It is also quite interesting that this wind does not require excessive thermal or cosmic-ray pressures (both pressures are not extreme compared to what has been estimated for the inner Milky Way), nor does this simple model require much more energy than the standard inferred supernova rate implies. Taking this result at face value, such a wind would be very important to the “ecology” of the Milky Way due to the high mass loss rate of $2 M_\odot \text{ yr}^{-1}$. In addition, such a wind would also play an important role in removing angular momentum from matter in the Galactic disk and allowing matter to move radially inward (Zirakashvili et al. 1996). At the least, this shows that such wind models should be considered further for the Milky Way; they may be able to explain at least a substantial fraction of the observed soft X-ray emission.

Further, as other researchers have already shown (Breitschwerdt et al. 2002), such winds can also be used to explain the unexpectedly slow rise in γ -ray emission towards the center of the Galaxy; this work therefore gives independent support to the Galactic wind hypothesized in Breitschwerdt et al. (2002). We have not yet calculated the effect of the best-fit wind model on the cosmic-ray distribution, but a simple approximation will investigate if this wind is removing cosmic rays at too high a rate. We reason as follows. The best-fit wind model shown here has a cosmic-ray advective timescale of $\sim 4.3 \times 10^6$ years. Therefore, supernova in the disk must resupply the cosmic-ray pressure on that timescale. We know that the approximate total supernova energy in the disk (from observations, see §4.2) is $\sim 1.7 \times 10^{41} \text{ ergs s}^{-1}$. So, if some fraction of this energy, ϵ_{CR} , is given to cosmic rays, and dis-

tributed over the volume occupied by hot gas where the wind is launched (over the Galactocentric radius range of 1.5 to 4.5 kpc, and a height range of ± 2 kpc, to be conservative), that energy density should be similar to the cosmic-ray pressure required to launch the wind. Calculating the resultant buildup of P_c over 4.3×10^6 years at the observed SN rate, we find $P_c \sim \epsilon_{CR} \cdot 6.9 \times 10^{-12} \text{ dyne cm}^{-2}$ or $\sim \epsilon_{CR} \cdot 5.0 \times 10^4 \text{ K cm}^{-3}$. This is actually of order the P_c that the best-fit model requires (see Table 2), although it would require $\epsilon_{CR} \sim 0.6$ to duplicate the best-fit P_c , which is relatively high. Still, this simple, rather conservative calculation shows that the high \dot{M} wind shown here does not remove cosmic rays much more quickly than they can be replenished by the normal SN rate in the Galaxy, although the removal rate of cosmic rays is certainly non-negligible, and would affect the density of cosmic rays towards the Galactic center. Of course, a more detailed calculation is required (with a more detailed wind model), but this again shows that the best-fit wind model is at least feasible, and would have a significant but not destructive effect on the Galaxy’s cosmic-ray density.

5.1. Future Improvements

More detailed models are clearly needed; there are a few concerns about the current model that could be addressed with more realistic wind models. For instance, we have assumed uniform density at the base of the wind over the area of the disk from $R = 1.5$ kpc to 4.5 kpc, which leads to a mass outflow rate of order $2 M_\odot \text{ yr}^{-1}$. This seems quite high, but in the context of a more detailed model with variations in density within the wind, we might expect that the n^2 weighting of emissivity would favor overdensities, and allow an inhomogeneous wind to better reproduce the observations with a smaller mass outflow rate. In addition, it is possible that other effects limit the gas to velocities below those in this simple model; drag effects may slow down the wind (e.g., Everett & Murray 2007), and could lead to some of the gas forming part of the Galactic fountain (Bregman 1999). On the other hand, turbulence may be an important additional source of energy for the wind, but we have not included such an input in this work. Also, the effects of distributed mass loading, which could be relatively easily incorporated into this model, have been ignored so far; such mass loading would be very important to the emission properties of the wind, and the potential observability of such winds in many galaxies. Finally, note that we have used Anders & Grevesse (1989) abundances; if the wind starts out with super-solar abundances (particularly in oxygen), a smaller mass outflow rate would be required.

The cosmic ray physics in this wind is still quite simple. As mentioned previously, we have assumed zero diffusivity of the cosmic rays throughout the wind (c.f., Breitschwerdt et al. 1993). We have also neglected thermal conductivity (our calculations show that conductivity may be important for $z \lesssim 350$ pc). Including both of these effects would be essential to future progress for this wind model: as mentioned previously (see §4.2), including the effects of conduction may help lower the energy requirements in the wind, bringing the total power of the wind closer to that of the total inferred supernovae power in the Galactic disk below the wind. We also note that we are using a model of the gravitational potential that we know overestimates the potential in the Milky Way (see §2). Adopting the more detailed potential model of Dehnen & Binney (1998) may allow a lower total-energy wind to duplicate the soft X-ray observations. Finally, we have also assumed the hydrodynamic model of McKenzie &

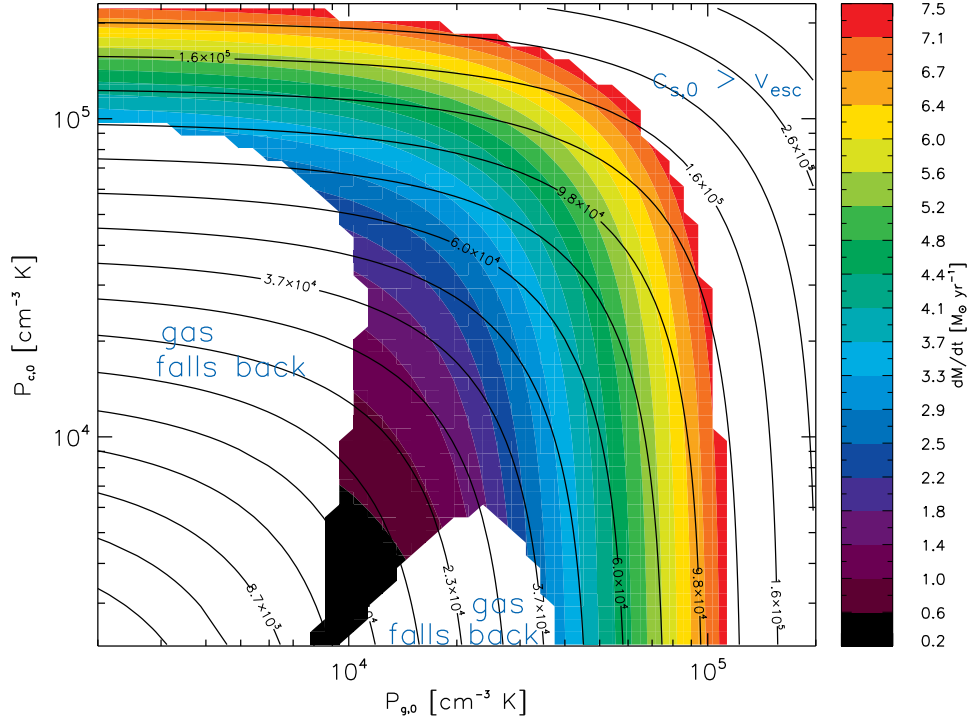


FIG. 11.— Mass loss in the wind vs. changes in the initial cosmic-ray pressure and gas pressure. The black contour lines represent lines of constant total pressure. The winds in the shaded region of the contour plot represent mass loss in outflows that pass through a critical point; the unshaded regions show locations of parameter space where winds cannot be launched (where the total pressure is too low) or “evaporative” flows that do not pass through a critical point (at very high total pressure). For winds in this survey, R_0 , z_0 , n_0 , B_0 , z_{break} , and α (see Table 2) were fixed.

Webb (1984) and Breitschwerdt et al. (1991) for the interaction of cosmic rays with Alfvén waves and the gas. To further examine this model, we will next consider the effects of higher cosmic-ray fluxes (Zweibel 2003) and apply it in other settings.

5.2. Future Tests

How can we further test this model? In analogy to early studies of the solar wind, this outflow may impact clouds in the vicinity of the galaxy, perhaps causing “comet-tail” extensions to high velocity clouds above the plane of the Milky Way. The formation of such “tails” would depend on the velocity of the wind. This has been studied in some detail before (Benjamin & Cox 2002), but should be reconsidered in the context of the predictions of these winds. In addition, it may be possible to study the kinematic impact of this wind on, for instance, the Magellanic Stream (A. Burkert, personal communication).

Another way to test the model would be to compare the wind with absorption columns and emission spectra towards the center of the Galaxy. Concerning absorption measurements, recent *Chandra* observations (Futamoto et al. 2004) towards the low-mass X-ray binary 4U 1820-303 show significant columns in O VII, O VIII, and Ne IX. As this X-ray binary is located within ten degrees of the Galactic center, at a distance of approximately 7.6 kpc, it seems an ideal target. However, similar absorption columns are found towards objects on sightlines that do not intercept the base of the wind; for instance, Mrk 421 shows similar absorption columns (Futamoto et al. 2004), but is far out of the plane. This leads us to conclude that the observed absorption is somewhat local to the Sun’s position, and, as such, this absorption does not

constrain the wind model. However, recent *Suzaku* measurements of emission at various latitudes along different sightlines towards the Galactic center (Rocks, 2008, in preparation) may help constrain the properties of the wind.

Finally, these winds, including their important cosmic-ray component, will also emit synchrotron radiation. We are now calculating the synchrotron emission expected from these wind models (Schiller et al., 2008, in preparation). This will allow exploration of the wind’s synchrotron emission as compared to recent models of Galactic synchrotron which begin to map the three-dimensional cosmic-ray emissivity (Nord et al. 2006).

Looking at a wider field of application, such wind models may also be quite important in application to starburst galaxies (e.g., Gallagher & Smith 2005; Socrates et al. 2006) and dwarf galaxies. The general applicability of these kinds of models to starbursting galaxies has been shown by Breitschwerdt (2003) in fitting cosmic-ray and thermally driven wind models to NGC 3079.

The initial impetus, in our group, for the investigation of a large-scale Galactic wind came from Dr. Don Cox; we are indebted to him for bringing the idea to our attention, and for various helpful conversations as the model was being developed. We thank the referee, Dr. Dieter Breitschwerdt, for his thorough reading of the paper and insightful comments and questions. We also thank Dr. Richard Almy for the development of the initial version of the code to map X-ray emission from the wind for comparison with *ROSAT* data. Finally, we thank Sebastian Heinz and Andreas Burkert for helpful comments and conversations. This work was supported by

NSF AST-0507367 and NSF PHY-0215581 (to the Center for Magnetic Self-Organization in Laboratory and Astrophysical

Plasmas) and NASA ATP grant NAG5-12128 (RAB). This research has made use of NASA's Astrophysics Data System.

REFERENCES

- Almy, R. C., McCammon, D., Digel, S. W., Bronfman, L., & May, J. 2000, *ApJ*, 545, 290
- Anders, E., & Grevesse, N. 1989, *Geochim. Cosmochim. Acta*, 53, 197
- Benjamin, R., & Cox, D. 2002, in *Bulletin of the American Astronomical Society*, Vol. 34, 1188+
- Benjamin, R. A., Benson, B. A., & Cox, D. P. 2001, *ApJ*, 554, L225
- Bloemen, H. 1989, *ARA&A*, 27, 469
- Bloemen, J. B. G. M., Blitz, L., & Hermsen, W. 1984, *ApJ*, 279, 136
- Bloemen, J. B. G. M., Dogiel, V. A., Dorman, V. L., & Ptuskin, V. S. 1993, *A&A*, 267, 372
- Bregman, J. N. 1999, in *Astronomical Society of the Pacific Conference Series*, Vol. 166, *Stromlo Workshop on High-Velocity Clouds*, ed. B. K. Gibson & M. E. Putman, 88+
- Breitschwerdt, D. 2003, in *Revista Mexicana de Astronomia y Astrofisica Conference Series*, ed. J. Arthur & W. J. Henney, 311–316
- Breitschwerdt, D., Dogiel, V. A., & Völk, H. J. 2002, *A&A*, 385, 216
- Breitschwerdt, D., McKenzie, J. F., & Völk, H. J. 1991, *A&A*, 245, 79 (BMV91)
- . 1993, *A&A*, 269, 54
- Breitschwerdt, D., & Schmutzler, T. 1994, *Nature*, 371, 774
- . 1999, *A&A*, 347, 650
- Breitschwerdt, D., Völk, H. J., & McKenzie, J. F. 1987, in *Interstellar Magnetic Fields: Observation and Theory*, ed. R. Beck & R. Graeve, 131–141
- Chandran, B. D. G. 2000, *Physical Review Letters*, 85, 4656
- Cho, J., & Vishniac, E. T. 2000, *ApJ*, 539, 273
- Cordes, J. M., & Lazio, T. J. W. 2002, *ArXiv Astrophysics e-prints*
- Cox, D. P. 2005, *ARA&A*, 43, 337
- Dehnen, W., & Binney, J. 1998, *MNRAS*, 294, 429
- Dickey, J. M., & Lockman, F. J. 1990, *ARA&A*, 28, 215
- Drury, L. O., & Völk, H. J. 1981, *ApJ*, 248, 344
- Ensslin, T. A., Pfrommer, C., Springel, V., & Jubelgas, M. 2006, *ArXiv Astrophysics e-prints*
- Everett, J. E., & Murray, N. 2007, *ApJ*, 656, 93
- Faucher-Giguère, C.-A., & Kaspi, V. M. 2006, *ApJ*, 643, 332
- Feldmeier, A., Shlosman, I., & Vitello, P. 1999, *ApJ*, 526, 357
- Ferrière, K. M. 2001, *Reviews of Modern Physics*, 73, 1031
- Futamato, K., Mitsuda, K., Takei, Y., Fujimoto, R., & Yamasaki, N. Y. 2004, *ApJ*, 605, 793
- Gallagher, J. S., & Smith, L. J. 2005, in *Astronomical Society of the Pacific Conference Series*, Vol. 331, *Extra-Planar Gas*, ed. R. Braun, 147+
- Goldreich, P., & Sridhar, S. 1995, *ApJ*, 438, 763
- Hasinger, G., Burg, R., Giacconi, R., Hartner, G., Schmidt, M., Trumper, J., & Zamorani, G. 1993, *A&A*, 275, 1
- Hindmarsh, A. C. 1983, in *Scientific Computing*, ed. e. a. Steplemen, R. S., 55–64
- Ipavich, F. M. 1975, *ApJ*, 196, 107
- Kashyap, V., Rosner, R., Micela, G., Sciortino, S., Vaiana, G. S., & Harnden, Jr., F. R. 1992, *ApJ*, 391, 667
- Kopp, R. A., & Holzer, T. E. 1976, *Sol. Phys.*, 49, 43
- Kulsrud, R., & Pearce, W. P. 1969, *ApJ*, 156, 445
- Kulsrud, R. M. 2005, *Plasma physics for astrophysics (Plasma physics for astrophysics / Russell M. Kulsrud. Princeton, N.J. : Princeton University Press, c2005. (Princeton series in astrophysics))*
- Kulsrud, R. M., & Cesarsky, C. J. 1971, *Astrophys. Lett.*, 8, 189
- Lazarian, A. 2006, *Astronomische Nachrichten*, 327, 609
- Leer, E., & Holzer, T. E. 1980, *J. Geophys. Res.*, 85, 4681
- Lorimer, D. R., Faulkner, A. J., Lyne, A. G., Manchester, R. N., Kramer, M., McLaughlin, M. A., Hobbs, G., Possenti, A., Stairs, I. H., Camilo, F., Burgay, M., D'Amico, N., Corongiu, A., & Crawford, F. 2006, *MNRAS*, 372, 777
- Lyne, A. G., Manchester, R. N., & Taylor, J. H. 1985, *MNRAS*, 213, 613
- McKenzie, J. F., & Webb, G. M. 1984, *Journal of Plasma Physics*, 31, 275
- Milano, L. J., Matthaeus, W. H., Dmitruk, P., & Montgomery, D. C. 2001, *Physics of Plasmas*, 8, 2673
- Nord, M. E., Henning, P. A., Rand, R. J., Lazio, T. J. W., & Kassim, N. E. 2006, *AJ*, 132, 242
- Park, S., Finley, J. P., & Dame, T. M. 1998, *ApJ*, 509, 203
- Park, S., Finley, J. P., Snowden, S. L., & Dame, T. M. 1997, *ApJ*, 476, L77+
- Ptuskun, V. S., Völk, H. J., Zirakashvili, V. N., & Breitschwerdt, D. 1997, *A&A*, 321, 434
- Ptuskun, V. S., & Zirakashvili, V. N. 2003, *A&A*, 403, 1
- Raymond, J. C., & Smith, B. W. 1977, *ApJS*, 35, 419
- Schmitt, J. H. M. M., & Snowden, S. L. 1990, *ApJ*, 361, 207
- Shebalin, J. V., Matthaeus, W. H., & Montgomery, D. 1983, *Journal of Plasma Physics*, 29, 525
- Skilling, J. 1975, *MNRAS*, 172, 557
- Smith, R. K., Brickhouse, N. S., Liedahl, D. A., & Raymond, J. C. 2001, *ApJ*, 556, L91
- Snowden, S. L., Egger, R., Freyberg, M. J., McCammon, D., Plucinsky, P. P., Sanders, W. T., Schmitt, J. H. M. M., Truemper, J., & Voges, W. 1997, *ApJ*, 485, 125
- Snowden, S. L., Freyberg, M. J., Plucinsky, P. P., Schmitt, J. H. M. M., Truemper, J., Voges, W., Edgar, R. J., McCammon, D., & Sanders, W. T. 1995, *ApJ*, 454, 643
- Socrates, A., Davis, S. W., & Ramirez-Ruiz, E. 2006, *ArXiv Astrophysics e-prints*
- Strong, A. W., Moskalenko, I. V., Reimer, O., Digel, S., & Diehl, R. 2004, *A&A*, 422, L47
- Veilleux, S., Cecil, G., & Bland-Hawthorn, J. 2005, *ARA&A*, 43, 769
- Wentzel, D. G. 1968, *ApJ*, 152, 987
- Wolfire, M. G., McKee, C. F., Hollenbach, D., & Tielens, A. G. G. M. 2003, *ApJ*, 587, 278
- Yan, H., & Lazarian, A. 2003, *ArXiv Astrophysics e-prints*
- . 2005, *ArXiv Astrophysics e-prints*
- Zirakashvili, V. N., Breitschwerdt, D., Ptuskun, V. S., & Völk, H. J. 1996, *A&A*, 311, 113
- Zweibel, E. G. 2003, *ApJ*, 587, 625